Layer-wise Spatial Modeling of Porosity in Additive Manufacturing

Jia (Peter) Liu[1], Chenang Liu[1], Yun Bai[2], Prahalad Rao[3], Chris Williams[2], Zhenyu (James) Kong[1*]

[1]Grado Department of Industrial and Systems Engineering, Virginia Tech

[2]Department of Mechanical Engineering, Virginia Tech

[3] Department of Mechanical and Materials Engineering, University of Nebraska-Lincoln

Abstract

The objective of this work is to model and quantify the layer-wise spatial evolution of porosity in parts made using additive manufacturing (AM) processes. This is an important research area because porosity has a direct impact on the functional integrity of AM parts such as their fatigue life and strength. To realize this objective, an augmented layer-wise spatial log Gaussian Cox process (ALS-LGCP) model is proposed. The ALS-LGCP approach quantifies the spatial distribution of pores within each layer of the AM part and tracks their sequential evolution across layers. Capturing the layer-wise spatial behavior of porosity leads to a deeper understanding of where (at what location), when (at which layer), and to what severity (size and number) pores are formed. This work therefore provides a mathematical framework for identifying specific pore-prone areas in an AM part, and tracking the evolution of porosity in AM parts in a layer-wise manner. This knowledge is essential for initiating remedial corrective actions to avoid porosity in future parts, e.g., by changing the process parameters or part design. The ALS-LGCP approach proposed herein is a significant improvement over the current scalar metric used to quantify porosity, namely, the percentage porosity relative to the bulk part volume. In this paper, the ALS-LGCP approach is tested for metal parts made using a binder jetting AM process to model the layer-wise spatial behavior of porosity. Based on offline, non-destructive X-Ray computed tomography (XCT) scan data of the part the approach identifies those areas with high risk of porosity with statistical fidelity approaching 85% (F-score). While the proposed work uses offline XCT data, it takes the critical first-step from a data analytics perspective for taking advantage of the recently reported breakthroughs in online, *in-situ* X-Ray-based monitoring of AM processes. Further, the ALS-LGCP approach is readily extensible for porosity analysis in other AM processes; our future forays will focus on improving the computational tractability of the approach for online monitoring.

Key words: Additive Manufacturing, Binder Jetting, Porosity, Layer-wise Porosity Modeling, X-Ray Computed Tomography (XCT), Log Gaussian Cox Process, Layer-wise Spatial Analysis.

*Corresponding author

1. Introduction

1.1 Motivation

The potential of additive manufacturing (AM) to transcend design and material constraints of traditional subtractive and formative manufacturing processes has been conclusively demonstrated in the preceding decade [1]. For instance, functional metal AM parts made from Inconel and Titanium are entering service in aerospace and biomedical industries [1]. Despite its transformative potential, the wider use of AM is encumbered due to poor process repeatability and frequent occurrence of various types of build defects which curtail the functional integrity of the part, such as strength and fatigue life [2, 3]. In the context of defects, the following types of AM defects have attracted the most attention: porosity, surface finish, cracking, layer delamination, and geometric distortion [3, 4]. This work focuses on understanding the evolution of porosity in a specific type of AM process called binder jetting, which is also called 3D Printing (3DP), by spatial modeling of the pores across multiple layers [5].

A salient aspect of AM is that the raw material is deposited and formed simultaneously layer-by-layer. Hence, not only does the integrity of certain areas impacts that of adjacent areas within the same layer, but also the integrity of the previous layer influences subsequent layers [2, 4]. The within-layer and across-layer dependence of porosity in AM has not been quantified before. Currently, a common quantifier for porosity in AM parts is the percentage porosity relative to the bulk volume of the part. Percentage porosity does not reveal the underlying pattern by which pores form and propagate across layers [6]. This knowledge is the critical first-step towards initiating offline or online corrective actions to improve product quality by either changing the process parameters or the part design.

1.2 Objective

The objective of this work is to quantify and model the layer-wise spatial evolution and distribution of porosity in AM parts by developing an augmented layer-wise spatial log Gaussian Cox process (ALS-LGCP) model based on offline XCT scan data. This model comprehensively evaluates the porosity of AM parts in a layer-wise manner, and subsequently, predicts the expected porosity in parts under current process conditions. ALS-LGCP is an integration of the spatial analysis on each layer in two dimensions (2D) and the sequential analysis across the consecutive layers (i.e. the third dimension). The approach uses XCT data to isolate where (at what 2D location), when (at which layer), and to what extent or severity (size and number) pores are formed. The ALS-LGCP is used in this work to understand the layer-wise spatial behavior of pores for parts made using binder jetting AM process.

The scientific rationale is that porosity attributes such as the number, location, size, form, and type of pores are intimately connected to distinctive process phenomena [4]. By tracking and quantifying these porosity attributes a deeper understanding of the causal process phenomena is obtained, and subsequently, from an offline monitoring perspective, the process parameters and design features can be optimized based on quantifying the layer-wise evolution of porosity formation [7, 8].

Recent breakthroughs concerning *in-situ* X-Ray diffraction-based imaging of process dynamics in powder bed fusion additive manufacturing have been reported in Refs. [9, 10] . Despite these significant recent developments, quantitative methods for systematically analyzing the XCT scan images towards understanding the layer-wise evolution of porosity remain largely unexplored [11, 12]. Although the work proposed in this manuscript was focused on offline spatial modeling of porosity distribution, instead of online monitoring, the developed knowledge will serve as a critical foundation for closed-loop process control as online X-Ray imaging techniques become more widely used in AM machines

in the near future. The work proposed in this paper lays the foundation from a data analytics perspective for taking advantage of these emerging in-situ X-ray imaging techniques for online analysis of porosity in AM.

1.3 Hypothesis

The central hypothesis is that the occurrence of pores is not independent, but, that there is a spatial correlation in the distribution of pores within each layer, and also a directional correlation in the distribution of pores from layer-to-layer. Hence, by modeling the correlation of porosity across sequential layers using the ALS-LGCP model, the occurrence of pores can be estimated within certain statistical confidence. This quantification is valuable for selecting the process parameter settings or making product design choices to reduce porosity in AM parts.

This hypothesis is tested in Sec. 4 in the context of the copper part made using binder jetting shown in Figure 1. The part design and a sample part are shown in Figure 1(a) and Figure 1(b), respectively. The part is printed in a direction normal to the plane of the page. The XCT scanner used in the experiments has the resolution ~50μm. Each XCT scan roughly corresponds one actual layer (~100μm) by aligning the scanning direction to the printing direction. Excessive pores are observed on the XCT scans of the cylindrical stem, therefore, the region of interest is defined as a square area (~7mm×7mm) on each layer within the cylindrical stem region, as shown in Figure 1(c) and Figure 1(d), respectively. It is observed from Figure 1(d) that pores tend to cascade across layers and occur repeatedly in certain regions, which supports the hypothesis that the spatial location of pores is correlated across layers.

The rest of the paper is structured as follows: a review of the pertinent literature is presented in Sec. 2; the proposed ALS-LGCP is detailed in Sec. 3; further corroboration of ALS-LGCP with a numerical case study and application to a copper part fabricated using binder jetting is presented in Sec. 4; and

conclusions and avenues for further research are summarized in Sec. 5.

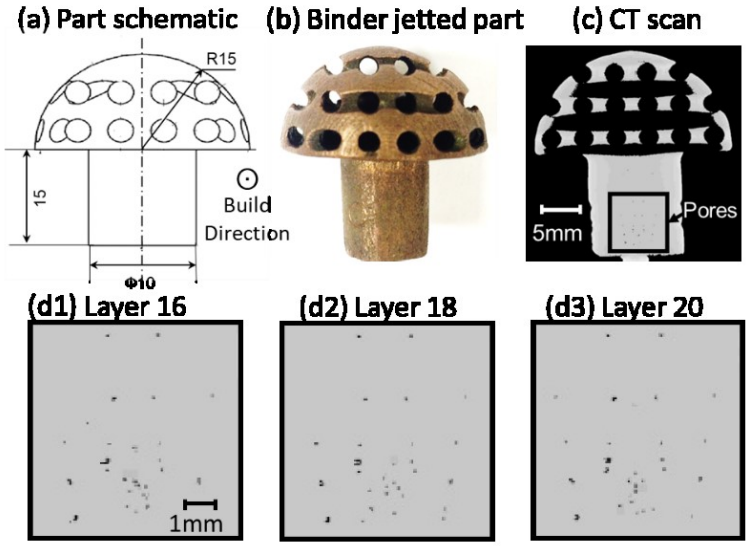

Figure 1: (a) A schematic of the part design in millimeter units (not to scale). (b) A copper part with intricate features fabricated using binder jetting. (c) XCT scan image with pores on the stem of the product. (d) Sequential zoomed images of pores on the stem of the part in layer 16, 17, and 18. It is noticed that the pores on these sequential layers are dependent within and across layers.

2. Review of the Related Research

This review is divided into two parts: (1) background on porosity in powder-based AM processes; and (2) summary of the point process statistical analysis which is at the root of the ALS-LGCP approach used for modeling the layer-wise spatial behavior of porosity in AM.

2.1 Background on porosity in powder-based AM processes

Porority is a frequent and prominent defect in powder-based AM processes, namely, directed energy deposition (DED), laser and electron beam powder bed fusion (LPBF and EPBF), and binder jetting (BJ)[4]. It has a negative influence on the mechanical performance of AM parts, leading to premature failure, and remains an impediment to wider application of AM processes [13, 14].

Porosity occurs typically due to: (a) the part design, (b) material properties, (c) machine-related errors, and (d) processing and environmental conditions [4]. For example, in powder bed fusion AM process, incomplete melting of particles from insufficient input energy leads to acicular pores at the

meso-scale (10 μm to 100 μm); while excessive energy leads to material vaporization and hence micro-level gas pores (< 10 μm) [7, 8, 15]. In ceramic or metal parts fabricated with binder jetting, pores are mainly generated due to low dosing of the powder bed, i.e., insufficient amount of powder is raked across the powder bed [16-18]. Since the nature of porosity is contingent on its root cause, thorough quantification of its attributes (type, size, form, and location) is a prerequisite for process improvement.

As a common practice, percentage porosity i.e., the percentage of pores relative to the bulk volume of the part, is used to quantify porosity in AM parts [13]. The porosity value is obtained by several well-established methods, such as Archimedes' method [19, 20], ultrasonic testing [13, 21], microscopic image analysis methods [22, 23], and X-ray computed tomography (XCT) [11, 24, 25]. While Archimedes' method is the preferred technique for assessing porosity, it provides no spatial and morphological information of porosity. In contrast, microscopic analysis and XCT methods capture the layer cross-section information. These techniques, apart from providing a volume measurement of porosity, can be used to analyze the morphological features and occurrence of pores [11, 24, 25].

The XCT method to assess porosity in AM parts provides non-destructive measurement of the internal morphology [11, 12, 26]. The application of XCT in AM can be traced back to the early nineties, when it was mainly used for reverse engineering purposes, and has gradually evolved since then as an established method for AM part qualification [27]. For instance, Taud *et al.* [28] measured overall percentage porosity in AM parts from XCT scans by calculating the ratio of the number of voxels representing pores to the number voxels representing the bulk material. Siddique *et al*. [11] applied dimensional measurements of individual pores from XCT scans in their characterization of fatigue performance. Likewise, Tammas-Williams *et al*. [12] identified areas of a part frequently afflicted with porosity from XCT scans by visualizing the pores in a reconstructed 3D space. However, investigation

of the distribution and propagation of pores within a layer and across different layers from XCT scan images, and the subsequent layer-wise identification of areas where pores are liable to occur, remain an open research problem.

As mentioned previously, two recent breakthroughs [9, 10] have been reported in online X-Ray imaging of laser powder bed fusion AM process. These works are primarily concerned with imaging the material phase transformations and meltpool solidification dynamics. Nonetheless, offline analysis of porosity in AM parts using digital image analysis of XCT scans is an actively research areas spanning national labs and industry [29]. However, the modeling framework proposed in this work is not merely restricted for analyzing the degree of porosity, but predicting their evolution. This knoweldge will serve as a critical foundation for closed-loop process control as online X-Ray imaging techniques become more widely used in AM machines in the near future.

2.2 Summary of point process analysis

This paper proposes a novel approach based on point process analysis to quantify porosity in AM parts from XCT scan images. As a component of spatial statistics, point process analysis aims to investigate the distribution-related characteristics and mutual dependence of events occurring within a defined region of interest [30, 31]. More specifically, point processes use dimensionless points to capture the number and the locations of events within a region of interest through a stochastic intensity function [30, 31].

Examples of point processes are common in the natural sciences, such as ecology and epidemiology [32, 33]. For instance, the spread of certain tree species (as events) in a forest (as the region of interest) [32]. The use of point process analysis has recently gained traction in manufacturing. For instance, Zhou *et al.* [34] used point process analysis to explain the clustering phenomena of

particles in the manufacture of nanocomposites. Likewise, Dong *et al.* [35] invoked point process modeling to quantify the mixing of nanoparticles within composite materials. However, the application of point process analysis for modeling porosity in AM remains unexplored.

Among point processes, spatiotemporal log Gaussian Cox process (ST-LGCP) is a hierarchical modeling approach [36, 37] which incorporates an additional dimension (i.e. time) to the spatial analysis in the 2D space. ST-LGCP models capture complex spatial heterogeneity and temporal correlation among events through a nonparametric intensity function that encapsulates a random process in space-time. It is the latest embodiment in spatiotemporal point process analysis and has been widely applied into different applications with historical data of event occurrence. For instance, in healthcare, research of spatiotemporal analysis with LGCP progresses for disease surveillance and control by modeling the spreading of different diseases along space and time [38-40]; in crime oversight, ST-LGCP methodology quantifies the risks with the correlation of contagion and history from the crime data and security data [41]; in natural disaster prevention, e.g. wild fires [42], earthquakes [43], the risk areas are located from the spatiotemporal pattern of the nature disasters learned from historical data.

If applied in modeling layer-wise porosity for AM parts with the time dimension representing the layer-wise direction, a prominent aspect of ST-LGCP is that it reduces events within the region of interest to dimensionless points by disregarding the morphological aspects (form and size) of the events. Accordingly, ST-LGCP introduces a bias which is magnified in the modeling of porosity in AM, because, pores in AM parts have different sizes and shapes contingent on the causal process phenomena. For example, in powder bed fusion, gas pores which are largely spherical occur at the micro-scale (< 10 μm), while elongated acicular pores occur at the meso-scale (10 μm to 100 μm) [3]. Disregarding the effect of pore morphology (size and form) is therefore not physically tenable and will inevitably lead to

inaccurate quantification of porosity [35].

In this paper, the framework of ST-LGCP is further improved to incorporate the pore morphology in the modeling from the selected XCT scans, consequently, an augmented layer-wise spatial log Gaussian Cox process (ALS-LGCP) is developed to investigate the layer-wise evolution of pores and predict the porosity-prone areas on the different layers in AM parts. The LS-LGC framework proposed in this work overcomes this inherent morphology-related limitation of ST-LGCP by formulating the sequential spatial distribution of pores on different layers through an augmented point pattern that considers the morphological features (size and form) of pores.

3. Proposed Research Methodology

The framework of the overall research methodology is summarized in Figure 2. The proposed ALS-LGCP methodology for layer-wise porosity modeling includes four basic steps:

Step 1 (Sec. 3.2): Pores on each XCT scan image (i.e., a layer) are represented by augmented point patterns.

Step 2 (Sec. 3.3 and Sec. 3.4): ALS-LGCP is formulated for sequential spatial analysis on layer-wise porosity.

Step 3 (Sec. 3.5): Parameters for ALS-LGCP are estimated using the Metropolis-Adjusted Langevin algorithm (MALA).

Step 4 (Sec. 3.6) Validation of ALS-LGCP is implemented by extrapolating porosity-prone areas on next layer.

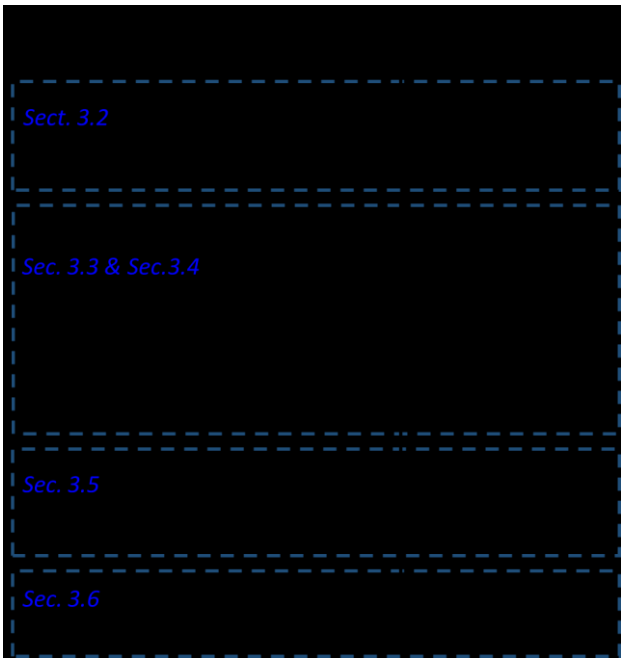

Figure 2: Overall methodology of ALS-LGCP for layer-wise porosity modeling and prediction.

Key notations that appear in the following sections are summarized in Table 1.

Table 1: Nomenclature and notations used in this work.

$\boldsymbol{W}$	The region of interest, $\boldsymbol{W} \subseteq \mathbb{R}^d$
$\boldsymbol{u}$	Spatial location of a pore, $\boldsymbol{u} \in \boldsymbol{W}$
$\boldsymbol{r}$	Morphology of a pore, defined as a matrix representing the circumscribed rectangle of a pore, with element equal to 1 if the corresponding pixel belongs to the pore.
t	Layer number of the sequential images of an AM part, $t \in [1, \mathrm{T}]$, T is the total layer number
n_t	Number of the pores in an augmented point pattern on layer t
$\boldsymbol{Z}_t$	Augmented point pattern in the region of interest $\boldsymbol{W}$ on layer t with n_t pores at locations $\boldsymbol{u}_1, \boldsymbol{u}_2, \dots, \boldsymbol{u}_{n_t}$
$\boldsymbol{Y}_t$	A realization from the Gaussian process in ALS-LGCP on layer t
$\mathbf{X}$	Covariate of the realization in the Gaussian process
$\boldsymbol{\beta}$	Parameters for the covariates in the Gaussian process
$C_{\boldsymbol{Y}}$	Covariance function in the Gaussian process
σ^2	Variance parameter in the covariance matrix for the Gaussian process
ϕ	Spatial scale parameter in the covariance matrix for the Gaussian process
θ	Layer-wise directional scale parameter in the covariance matrix for the Gaussian process
$\boldsymbol{\Lambda}_t$	Intensity function for the augmented point patterns in ALS-LGCP on layer t
$\bar{\mathrm{f}}_t$	Average severity parameter representing the average size of the points within the region of interest $\boldsymbol{W}$ on layer t
$\mathrm{D}_{i,j}$	The (i, j) cell in the discretization over the region of interest $\boldsymbol{W}$
M	The number of rows (or columns) in the discretized region of interest

$\widetilde{\boldsymbol{Z}}_t$	Discretized point pattern on layer t, restructured as a $\mathrm{M} \times \mathrm{M}$ vector, with elements $\tilde{Z}_{(i,j),t}$ in cell $\mathrm{D}_{i,j}$
$\widetilde{\boldsymbol{Y}}_t$	Discretized random realization from the Gaussian process in ALS-LGCP on layer t, restructured as a $\mathrm{M} \times \mathrm{M}$ vector, with elements $\tilde{Y}_{(i,j),t}$ in cell $\mathrm{D}_{i,j}$

3.1 Introduction to spatiotemporal log Gaussian Cox process (ST-LGCP) modeling

ST-LGCP is defined as a hierarchical model, the first-level of which is a Gaussian process (GP) that accommodates a nonparametric intensity function $\boldsymbol{\Lambda}_t$, where t is an AM part layer and $\boldsymbol{Y}_t$ is a realization from the GP [36, 37].

$$\boldsymbol{\Lambda}_t = \exp(\boldsymbol{Y}_t) \tag{1}$$

$$\boldsymbol{Y}_t \sim \mathrm{GP}(\mathbf{X}'\boldsymbol{\beta}, C_{\boldsymbol{Y}}) \tag{2}$$

where mean $\mathrm{E}(\boldsymbol{Y}_t) = \mathbf{X}'\boldsymbol{\beta}$, $\mathbf{X}$ is the covariate of the realization $\boldsymbol{Y}_t$ $(t = 1, \ldots, \mathrm{T})$, T is the number of layers, $\boldsymbol{\beta}$ is the parameter for the covariates. The covariance function $C_{\boldsymbol{Y}}$ is typically represented as a distance-based kernel function with an assumption that shorter distances result in higher correlations. The radial basis function is a popular choice due to its compact form, involving only three parameters, namely, variance (σ^2), spatial scale parameter (ϕ) and temporal scale parameter (θ). Accordingly, a separable spatiotemporal covariance function can be written as follows [30],

$$C_{\boldsymbol{Y}}\big((\boldsymbol{u}, t), (\boldsymbol{s}, v)\big) = \mathrm{cov}[Y_t(\boldsymbol{u}), Y_v(\boldsymbol{s})] = \sigma^2 \exp\left(-\frac{\|\boldsymbol{u} - \boldsymbol{s}\|}{\phi}\right) \exp\left(-\frac{|t - v|}{\theta}\right) \tag{3}$$

where $\boldsymbol{u}$ and $\boldsymbol{s}$ are two locations within the region of interest $\boldsymbol{W}$ on the layers t and v of XCT scan images, respectively, $(\boldsymbol{u}, t) \in \boldsymbol{W} \times [1, \mathrm{T}]$, $(\boldsymbol{s}, v) \in \boldsymbol{W} \times [1, \mathrm{T}]$.

In the second-level of ST-LGCP, a spatiotemporal point process $\boldsymbol{Z}_t$ is used to model the point pattern data on layer t. Conditional on the intensity function $\boldsymbol{\Lambda}_t$ from the first level formulated by Eq. (1), the spatiotemporal point process $\boldsymbol{Z}_t$ for the layer-wise porosity modeling is an inhomogeneous Poisson process on the layer t,

$$\boldsymbol{Z}_t \sim \mathrm{Possion}[\boldsymbol{\Lambda}_t] \tag{4}$$

with the expected number of pores on the layer t image as,

$$\mathrm{E}[n_t|\boldsymbol{\Lambda}_t] = \int_{\boldsymbol{u}\in\boldsymbol{W}} \Lambda_t(\boldsymbol{u})d\boldsymbol{u}, \tag{5}$$

3.2 Data representation by augmented point pattern

Before proceeding to the details of the proposed ALS-LGCP, augmented point pattern and average severity parameter are defined.

Definition 1 (Augmented point pattern): An augmented point pattern is a set of spatial pairs $\{(\boldsymbol{u}_i, \boldsymbol{r}_i) : i = 1, \cdots, n\}$ depicting the pore i in a region of interest $\boldsymbol{W}$ with its centroid coordinate $\boldsymbol{u}_i$ and its morphology $\boldsymbol{r}_i$. n is the number of pores in the region of interest $\boldsymbol{W}$.

The morphology $\boldsymbol{r}_i$ could take different formats to describe the morphological features of the pore, such as the size and the form. In this work, $\boldsymbol{r}_i$ is defined as a matrix representing the circumscribed rectangle of a pore, with element equal to 1 if the corresponding pixel belongs to the pore.

Figure 3 illustrates the use of augmented point pattern for a XCT scan from an AM part. While the XCT scan is a RGB image (Figure 3(a)), the augmented point pattern in Figure 3(b) represents a set of spatial pairs. To illustrate, a pore demarcated in Figure 3(b) is represented by a spatial pair $(\boldsymbol{u}, \boldsymbol{r})$ in the augmented point pattern, where location $\boldsymbol{u}$ is the centroid coordinate of the pore $\boldsymbol{u} = (29, 36)$, and morphology of the pore is translated as a matrix $\boldsymbol{r}$. Since the augmented point pattern has the morphological features (e.g., size and form) of pores, an average severity parameter is defined to quantify the detrimental impact of pores.

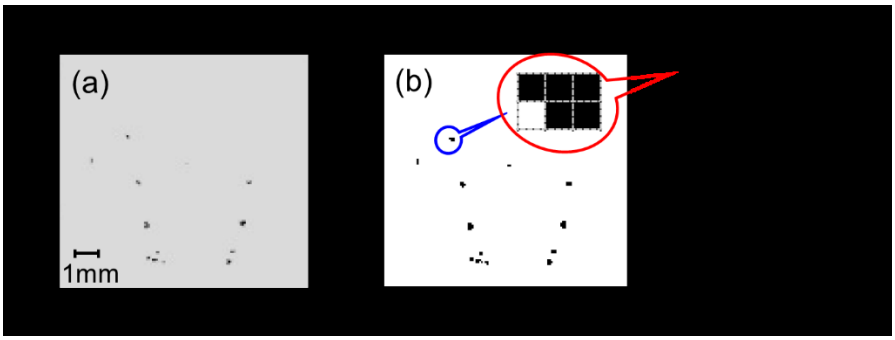

Figure 3: (a) An XCT scan image from a metal part manufactured by binder jetting. Pores are shown as dark spots in this RGB image (150×150 pixels). (b) The visualization of augmented point pattern for this XCT scan. Pores are represented by a set of spatial pairs with location and morphology. The pore in the circle occupies five pixels, and hence the information of its size and form is captured.

Definition 2 (Average severity parameter): An average severity parameter $\bar{\mathrm{f}}$ is defined as the average size (number of pixels) of all the pores within a region of interest $\boldsymbol{W} \subset \mathbb{R}^d$ on a layer. It is calculated from an augmented point pattern $\{(\boldsymbol{u}_i, \boldsymbol{r}_i) : i = 1, \cdots, n\}$ as,

$$\bar{\mathrm{f}} = \frac{1}{n}\sum_{i=1}^{n} \boldsymbol{e}_{\mathrm{R}}{}^{\mathrm{T}} \boldsymbol{r}_i \boldsymbol{e}_{\mathrm{C}} \tag{6}$$

where $\boldsymbol{e}_{\mathrm{C}}$ and $\boldsymbol{e}_{\mathrm{R}}$ are all-ones column vectors with lengths equal to the column number (n_{C}) and row number (n_{R}) of morphology $\boldsymbol{r}_i$, respectively. According to this definition, larger pores on a layer lead to higher average severity parameter, which is in alignment with practical observations [44].

It is noted that the calculation of average severity parameter transforms the morphology matrix $\boldsymbol{r}$ into the severity number. The severity numbers preserve the important size information of different pores, but it loses the information about the form of pores. In current applications with XCT scans of a binder jetted part as shown in Figure 1, the form of pores is not a differentiating factor due to their small size. Therefore, representing pore morphology with severity number in ALS-LGCP simplifies the computation and works sufficiently under current conditions. How to factor the form of pores in ALS-LGCP modeling will be investigated in future work for AM parts with larger pores.

When representing pores on the XCT scans as the augmented point patterns, they are generated from an inhomogeneous Poisson process conditional on a varying intensity function across the region of interest. For instance, the empirical estimate of the intensity function for the XCT scan of a binder jetted part (in Figure 4 (a)), calculated by using kernel method [31], is shown in in Figure 4 (b). The continuity of the estimated intensity function implies that the adjacent areas would have highly-correlated intensities. By using variogram [31], calculated empirical spatial correlation for the intensity

function in Figure 4 (c) further verifies the correlation depends on the distance. Therefore, in ALS-LGCP, a Gaussian process with a distance-based covariance is used to represent the intensity function of the augmented point patterns.

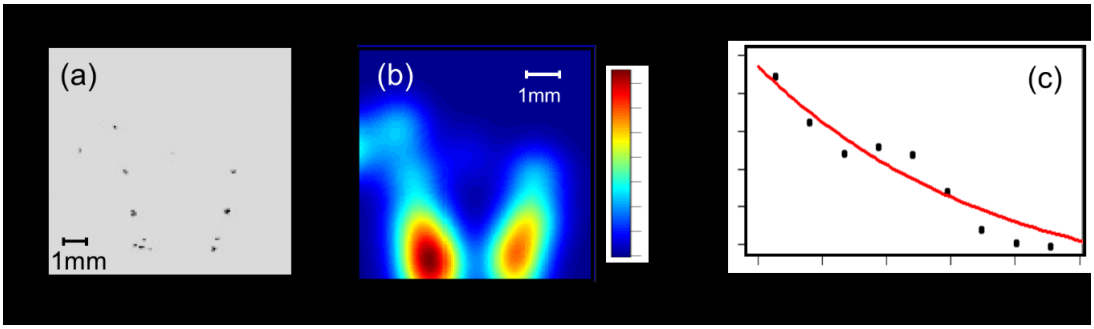

Figure 4: (a) An XCT scan image from a metal part manufactured by binder jetting as in Figure 3. Pores are shown as dark spots in this RGB image (150×150 pixels). (b) The empirical estimate of the intensity function obtained for the point pattern in (a) is continuous in the region of interest. (c) Empirical spatial correlation estimated from variogram shows the correlation decrease with the increase of distance.

3.3 Augmented Layer-wise spatial log Gaussian Cox process (ALS-LGCP)

The ALS-LGCP is defined as a hierarchical model; the first-level is to model the intensity function, which depicts the distribution-related characteristics in the augmented point pattern; the second-level is to model the augmented point pattern of pores.

In the first-level of ALS-LGCP, a Gaussian process (GP) is used to accommodate the complex form of a intensity function $\boldsymbol{\Lambda}_t$ for the augmented point pattern on the layer t in a nonparametric manner with its realization $\boldsymbol{Y}_t$ [36, 37]. The intensity function $\boldsymbol{\Lambda}_t$ can be calculated via a realization $\boldsymbol{Y}_t$ on the layer t as,

$$\boldsymbol{\Lambda}_t = \frac{\exp(\boldsymbol{Y}_t)}{\bar{\mathrm{f}}_t} \tag{7}$$

where $\bar{\mathrm{f}}_t$ is the average severity parameter for the layer t (see Definition 2), which denotes the average size of the pores on this layer.

In the second-level of ALS-LGCP, a layer-wise spatial point process $\boldsymbol{Z}_t$ on the layer t is used to model the augmented point pattern data. Conditional on the intensity function $\boldsymbol{\Lambda}_t$ from the first-level

formulated by Eq. (7), the spatial point process $\boldsymbol{Z}_t$ for the layer-wise porosity modeling is an inhomogeneous Poison process on the layer t,

$$\boldsymbol{Z}_t \sim \text{Possion}[\boldsymbol{\Lambda}_t] \tag{8}$$

with the expected number of pores on the layer t image as,

$$\text{E}[n_t|\boldsymbol{\Lambda}_t] = \int_{\boldsymbol{u}\in\boldsymbol{W}} \Lambda_t(\boldsymbol{u})d\boldsymbol{u} = \frac{\int_{\boldsymbol{u}\in\boldsymbol{W}} \exp\big(Y_t(\boldsymbol{u})\big)d\boldsymbol{u}}{\bar{\text{f}}_t} \tag{9}$$

3.4 Discretization of augmented layer-wise spatial log Gaussian Cox process (ALS-LGCP)

The proposed ALS-LGCP approach uses a Gaussian process to model the complex intensity function of augmented point patterns in a nonparametric manner. Despite its flexibility, the Gaussian process poses a computational challenge in spatial analysis for layer-wise porosity. Since the dimension of its realization $\boldsymbol{Y}_t$ as shown in Eq. (2) for layer t ($t = 1, \cdots, \text{T}$) depends on the number of pores on the particular layer, the computational complexity in tracking the pores across layers becomes untenable. To overcome this difficulty, the XCT scan images are discretized into cells [45, 46].

Discretizing a region of interest (e.g. a unit square) with $\text{M} \times \text{M}$ cells as shown in Figure 5. The cell on the row i and column j is represented as $\text{D}_{i,j} = \left[\frac{i-1}{\text{M}}, \frac{i}{\text{M}}\right] \times \left[\frac{j-1}{\text{M}}, \frac{j}{\text{M}}\right]$, $(i = 1,2, \dots, \text{M}, j = 1,2, \dots, \text{M})$, with the centroid $\tilde{\boldsymbol{u}}_{i,j} = (\frac{2i-1}{\text{M}}, \frac{2j-1}{\text{M}})$. With discretization, the observed point pattern $\boldsymbol{Z}_t$ within the region of interest on layer t is translated into an $\text{M} \times \text{M}$ matrix, in which each element $\tilde{Z}_{(i,j),t}$ $(i = 1,2, \dots, \text{M}, j = 1,2, \dots \text{M})$ represents the number of non-zero pixels from a certain pore in cell $\text{D}_{i,j}$. The $\text{M} \times \text{M}$ matrix can be reshaped as a vector $\widetilde{\boldsymbol{Z}}_t$. In the same vein, the realization of Gaussian process $\boldsymbol{Y}_t$ is discretized to a $\text{M} \times \text{M}$ matrix with elements $\tilde{Y}_{(i,j),t}$ $(i = 1,2, \dots, \text{M}, j = 1,2, \dots, \text{M})$, and then reshaped into a vector of a multivariate Gaussian random variable $\widetilde{\boldsymbol{Y}}_t$. The discretization facilitates the subsequent computation by making both $\widetilde{\boldsymbol{Z}}_t$ and $\widetilde{\boldsymbol{Y}}_t$ on all the layers $(t = 1, \cdots, \text{T})$ have the same dimension ($\text{M} \times \text{M}$). The choice of discretization is contingent on the

smoothness of the realizations of the Gaussian process.

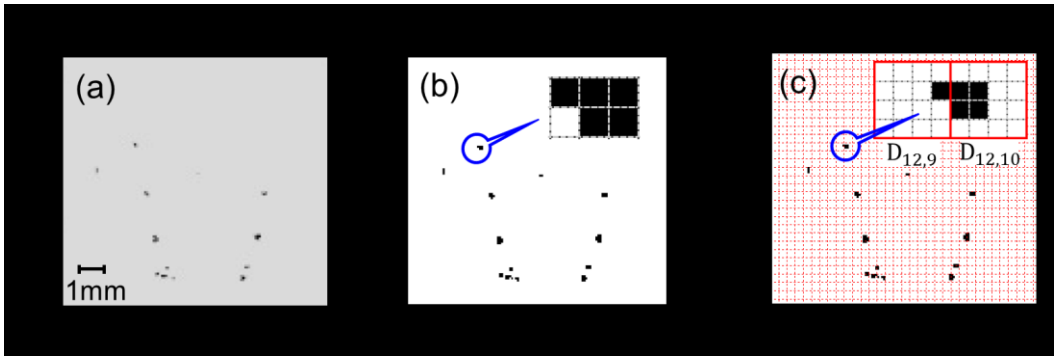

Figure 5: (a) An XCT scan image from a metal part manufactured by binder jetting. (b) The visualization of augmented point pattern for this XCT scan. A pore in the circle has five pixels, and hence the information of its size and form is captured by such a form of data representation. (c) After the discretization, the pore enclosed by the circle occupies two cells ($D_{12,9}$ and $D_{12,10}$), therefore, is represented by the discrete format of augmented point pattern ($\tilde{Z}_{(12,9)} = 1$ and $\tilde{Z}_{(12,10)} = 4$).

Due to discretization, a pore can occupy more than one cell depending on its size and form, in such a case it will be represented by the numbers of pixels in these cells together. That is, if a pore occupies two neighboring cells $D_{i,j}$ and $D_{i,j+1}$ on layer t, then $\tilde{Z}_{(i,j),t}$ and $\tilde{Z}_{(i,j+1),t}$ are used together to represent this pore. For instance, the augmented point pattern in Figure 5(b) is discretized with 38×38 cells with each cell including 16 pixels (Figure 5(c)), the pore $\{\boldsymbol{u} = (29, 36), \boldsymbol{r} = \begin{bmatrix} 1 & 1 & 1 \\ 0 & 1 & 1 \end{bmatrix}\}$ occupies two cells $D_{12,9}$ and $D_{12,10}$, and is represented by the number of pixels of the pore in these two cells together (one pixel and four pixels in these two cells, respectively, in this example), thus, assigning $\tilde{Z}_{(12,9)} = 1$ and $\tilde{Z}_{(12,10)} = 4$.

In the discretized ALS-LGCP for pore modeling, an exponential kernel is used to depicting correlation among random variables (e.g., $\tilde{Y}_{(i,j),t}$ and $\tilde{Y}_{(i,j+1),t}$, $(t = 1, \dots, \mathrm{T})$) in the latent Gaussian distribution representing cells $D_{i,j}$ and $D_{i,j+1}$ from XCT scans of AM parts. This leads to the following discretized format of ALS-LGCP model. The Gaussian process at the first-level is approximated by multivariate Gaussian distribution $\mathbb{N}(\cdot)$:

$$\tilde{\boldsymbol{Y}}_t \sim \mathbb{N}(\tilde{\mathbf{X}}'\boldsymbol{\beta}, C_{\tilde{Y}}) \tag{10}$$

where $\widetilde{\mathbf{X}}$ is the covariates of $\widetilde{\boldsymbol{Y}}_t$ on layer t $(t = 1, \dots, \mathrm{T})$ in the discretized format of ALS-LGCP model, and a separable layer-wise spatial covariance function is defined as

$$\begin{aligned} C_{\widetilde{\boldsymbol{Y}}}\left((\widetilde{\boldsymbol{u}}_{i,j}, t), (\widetilde{\boldsymbol{u}}_{i',j'}, t')\right) &= \mathrm{cov}\left[\tilde{Y}_{(i,j),t}, \tilde{Y}_{(i',j'),t'}\right] \\ &= \sigma^2 \exp\left(-\frac{\left\|\widetilde{\boldsymbol{u}}_{i,j} - \widetilde{\boldsymbol{u}}_{i',j'}\right\|}{\phi}\right) \exp\left(-\frac{|t - t'|}{\theta}\right) \end{aligned} \tag{11}$$

where (i, j) and (i', j') are the indices of cells occupied by pores $(i, i' = 1,2, \dots, \mathrm{M}, j, j' = 1,2, \dots, \mathrm{M})$ on the layer t and the layer t' respectively $(t, t' \in [1, \mathrm{T}])$. Denote $\eta = \{\sigma^2, \phi, \theta\}$ for notation simplicity in the MCMC algorithm in Sec. 3.5.

A spatial point process $\widetilde{\boldsymbol{Z}}_t$ for layer t is at the second-level with the intensity function

$$\widetilde{\boldsymbol{\Lambda}}_t = \frac{\exp(\widetilde{\boldsymbol{Y}}_t)}{\bar{\mathrm{f}}_t} \tag{12}$$

where $\bar{\mathrm{f}}_t$ is the average severity from Eq. (6) on layer t, which is estimated as the ratio between the number of pixels in pores and the number of pores ($\hat{n}_t$) on layer t:

$$\bar{\mathrm{f}}_t \approx \frac{1}{\hat{n}_t} \sum_{i=1}^{M} \sum_{j=1}^{M} \tilde{Z}_{(i,j),t} \tag{13}$$

Conditional on the intensity function $\widetilde{\boldsymbol{\Lambda}}_t$, the spatial point process $\widetilde{\boldsymbol{Z}}_t$ on layer t is expressed as an inhomogeneous Poisson point process as follows,

$$\widetilde{\boldsymbol{Z}}_t \sim \mathrm{Possion}\left[\widetilde{\boldsymbol{\Lambda}}_t\right] \tag{14}$$

and the expected number of pores in region $\boldsymbol{W}$ is calculated as

$$\mathrm{E}\left[n_t | \widetilde{\boldsymbol{\Lambda}}_t\right] \cong \sum_{i=1}^{\mathrm{M}} \sum_{j=1}^{\mathrm{M}} \tilde{\Lambda}_{(i,j),t} * \mathrm{C_A} \tag{15}$$

where $\tilde{\Lambda}_{(i,j),t}$ is the Poisson rate in the cell $\mathrm{D}_{i,j}$ at layer t, and $\mathrm{C_A}$ is the cell area in terms of pixels.

3.5 Parameter estimation in ALS-LGCP

Bayesian estimation is used to obtain the posterior distribution of the parameters from the prior belief functions of parameters and the observed augmented point patterns. This leads to a way for

estimating parameters in ALS-LGCP, which includes the parameters $(\eta, \boldsymbol{\beta})$ of the Gaussian process and the random process $\widetilde{\boldsymbol{Y}}_t$ (used for predicting the intensity function $\widetilde{\boldsymbol{\Lambda}}_t$ in the region of interest) in Eqs. (10) - (12) [45, 46].

Through layer-wise spatial discretization, the likelihood function of the augmented point patterns (to layer t) $\pi(\widetilde{\boldsymbol{Z}}_1, \dots, \widetilde{\boldsymbol{Z}}_t | \eta, \boldsymbol{\beta}, \widetilde{\boldsymbol{Y}}_t)$ and the priors $\pi(\eta, \boldsymbol{\beta}, \widetilde{\boldsymbol{Y}}_t)$ are obtained from finite dimensional distributions over the region of interest, enabling parameter estimation for the Gaussian process $(\eta, \boldsymbol{\beta})$ and prediction for the random process $\widetilde{\boldsymbol{Y}}_t$ in a Bayesian framework.

$$\begin{aligned} \pi(\eta, \boldsymbol{\beta}, \widetilde{\boldsymbol{Y}}_t | \widetilde{\boldsymbol{Z}}_1, \dots, \widetilde{\boldsymbol{Z}}_t) &\propto \pi(\widetilde{\boldsymbol{Z}}_1, \dots, \widetilde{\boldsymbol{Z}}_t | \eta, \boldsymbol{\beta}, \widetilde{\boldsymbol{Y}}_t) \pi(\eta, \boldsymbol{\beta}, \widetilde{\boldsymbol{Y}}_t) \\ &= \pi(\widetilde{\boldsymbol{Z}}_1, \dots, \widetilde{\boldsymbol{Z}}_t | \eta, \boldsymbol{\beta}, \widetilde{\boldsymbol{Y}}_t) \pi(\eta) \pi(\boldsymbol{\beta}) \pi(\widetilde{\boldsymbol{Y}}_t) \end{aligned} \tag{16}$$

Accordingly, $\pi(\widetilde{\boldsymbol{Y}}_t)$ is the corresponding finite dimensional Gaussian distribution on layer t, and the likelihood function $\pi(\widetilde{\boldsymbol{Z}}_1, \dots, \widetilde{\boldsymbol{Z}}_t | \eta, \boldsymbol{\beta}, \widetilde{\boldsymbol{Y}}_t)$ is a joint distribution of multiple Poisson distributions in the cells up to layer t. $\pi(\eta)$ and $\pi(\boldsymbol{\beta})$ are Gaussian distributions with mean and variance set as the estimated values from minimum contrast parameter estimation [46]. Consequently, the posterior distribution $\pi(\widetilde{\boldsymbol{Y}}_t | \widetilde{\boldsymbol{Z}}_1, \dots, \widetilde{\boldsymbol{Z}}_t)$ can be obtained by marginalizing η amd $\boldsymbol{\beta}$ in Eq. (16) [46].

A Metropolis-adjusted Langevin algorithm (MALA), a Markov chain Monte Carlo approach, is used to obtain sample-based estimate for the posterior distributions where the target distribution $\pi(\eta, \boldsymbol{\beta}, \widetilde{\boldsymbol{Y}}_t | \widetilde{\boldsymbol{Z}}_1, \dots, \widetilde{\boldsymbol{Z}}_t)$ is approximated by sequential samples $\left\{\eta^{(j)}, \boldsymbol{\beta}^{(j)}, \widetilde{\boldsymbol{Y}}_t^{(j)}\right\}_{j=1}^{N}$ from a Markov chain whose stationary distribution is the target [47, 48]. The design of the proposed density q herein is a mix of random walk and Langevin kernels. It is used to exploit the gradient information on the target to help guide movements towards areas of higher posterior probability [49]. The samples are drawn from the proposal density q and are accepted in a probabilistic way. For instance, in the *j*th step of the algorithm, a candidate $\{\eta^*, \boldsymbol{\beta}^*, \widetilde{\boldsymbol{Y}}^*\}$ is drawn from the proposal density

$\mathrm{q}\left(\eta^*, \beta^*, \widetilde{\boldsymbol{Y}}^* \middle| \eta^{(j-1)}, \beta^{(j-1)}, \widetilde{\boldsymbol{Y}}^{(j-1)}\right)$ and accepting it as the *j*th sample, i.e., setting $\left\{\eta^{(j)}, \beta^{(j)}, \widetilde{\boldsymbol{Y}}^{(j)}\right\}=\left\{\eta^*, \beta^*, \widetilde{\boldsymbol{Y}}^*\right\}$, with probability

$$\min\left\{1, \frac{\pi\left(\eta^*, \boldsymbol{\beta}^*, \widetilde{\boldsymbol{Y}}_t^* \middle| \widetilde{\boldsymbol{Z}}_1, \ldots, \widetilde{\boldsymbol{Z}}_t\right)}{\pi\left(\eta^{(j-1)}, \boldsymbol{\beta}^{(j-1)}, \widetilde{\boldsymbol{Y}}_t^{(j-1)} \middle| \widetilde{\boldsymbol{Z}}_1, \ldots, \widetilde{\boldsymbol{Z}}_t\right)} \frac{\mathrm{q}\left(\eta^{(j-1)}, \boldsymbol{\beta}^{(j-1)}, \widetilde{\boldsymbol{Y}}_t^{(j-1)} \middle| \eta^*, \boldsymbol{\beta}^*, \widetilde{\boldsymbol{Y}}_t^*\right)}{\mathrm{q}\left(\eta^*, \boldsymbol{\beta}^*, \widetilde{\boldsymbol{Y}}_t^* \middle| \eta^{(j-1)}, \boldsymbol{\beta}^{(j-1)}, \widetilde{\boldsymbol{Y}}_t^{(j-1)}\right)}\right\} \quad (17)$$

3.6 Validation of spatial porosity modeling across layers in ALS-LGCP

The validation of the layer-wise spatial porosity modeling with ALS-LGCP is implemented by choosing the next layer as the test dataset and predicting the pore-prone areas on the next layer. High prediction accuracy of porosity on the next layer would indicate the spatial dependence among consecutive layers are captured by the ALS-LGCP model. The one-layer prediction is also an illustration of the extrapolation capability of ALS-LGCP.

Represented in cells, the motive of the validation procedure here is to predict the multivariate Gaussian distribution of $\widetilde{\boldsymbol{Y}}_{\mathrm{T}+1}$ given the observed data $\left\{\widetilde{\boldsymbol{Z}}_1, \ldots, \widetilde{\boldsymbol{Z}}_{\mathrm{T}}\right\}$ up to layer T as in $\pi(\widetilde{\boldsymbol{Y}}_{\mathrm{T}+1}|\widetilde{\boldsymbol{Z}}_1, \ldots, \widetilde{\boldsymbol{Z}}_{\mathrm{T}})$, and consequently estimate the intensity function of observed augmented point patterns $\widetilde{\boldsymbol{\Lambda}}_{\mathrm{T}+1}$ with the mean of $\widetilde{\boldsymbol{Y}}_{\mathrm{T}+1}$ [45, 46]. A practical approach is to adopt recent observed data $\{\widetilde{\boldsymbol{Z}}_{\mathrm{T}-\mathrm{L}}, \ldots, \widetilde{\boldsymbol{Z}}_{\mathrm{T}}\}$, (L is a user-defined lag parameter), which have a bigger impact on the next observations, to predict the distribution $\pi(\widetilde{\boldsymbol{Y}}_{\mathrm{T}+1}|\widetilde{\boldsymbol{Z}}_{\mathrm{T}-\mathrm{L}}, \ldots, \widetilde{\boldsymbol{Z}}_{\mathrm{T}})$ [36]. The conditional independence properties of the model imply $\pi\left(\widetilde{\boldsymbol{Y}}_{\mathrm{T}+1}\middle|\widetilde{\boldsymbol{Z}}_{\mathrm{T}-\mathrm{L}}, \ldots, \widetilde{\boldsymbol{Z}}_{\mathrm{T}}\right)$ follows a multivariate normal distribution with mean

$$\mathrm{E}\left(\widetilde{\boldsymbol{Y}}_{\mathrm{T}+1}\middle|\widetilde{\boldsymbol{Z}}_{\mathrm{T}-\mathrm{L}}, \ldots, \widetilde{\boldsymbol{Z}}_{\mathrm{T}}\right) = \xi \mathrm{E}\left(\widetilde{\boldsymbol{Y}}_{\mathrm{T}}\middle|\widetilde{\boldsymbol{Z}}_{\mathrm{T}-\mathrm{L}}, \ldots, \widetilde{\boldsymbol{Z}}_{\mathrm{T}}\right) + (1-\xi)\widetilde{\mathbf{X}}'\boldsymbol{\beta} \quad (18)$$

and variance,

$$\mathrm{var}\left(\widetilde{\boldsymbol{Y}}_{\mathrm{T}+1}\middle|\widetilde{\boldsymbol{Z}}_{\mathrm{T}-\mathrm{L}}, \ldots, \widetilde{\boldsymbol{Z}}_{\mathrm{T}}\right) = \xi^2 \mathrm{var}\left(\widetilde{\boldsymbol{Y}}_{\mathrm{T}}\middle|\widetilde{\boldsymbol{Z}}_{\mathrm{T}-\mathrm{L}}, \ldots, \widetilde{\boldsymbol{Z}}_{\mathrm{T}}\right) + (1-\xi)^2 C_{\widetilde{\boldsymbol{Y}}} \quad (19)$$

where $\xi = \exp(-\theta)$ represents the sequential evolution of porosity across layers; $\pi\left(\widetilde{\boldsymbol{Y}}_{\mathrm{T}}\middle|\widetilde{\boldsymbol{Z}}_{\mathrm{T}-\mathrm{L}}, \ldots, \widetilde{\boldsymbol{Z}}_{\mathrm{T}}\right)$, viz., the distribution of $\widetilde{\boldsymbol{Y}}_{\mathrm{T}}$, can be estimated from Eq. (16) by MALA in Sec. 3.5.

The prediction of average severity on layer $\mathrm{T}+1$ ($\bar{\mathrm{f}}'_{\mathrm{T}+1}$) is obtained by exponential

smoothing[30], from (20) as follows with weight α,

$$\bar{\mathrm{f}}'_{\mathrm{T}+1} = \alpha\bar{\mathrm{f}}'_{\mathrm{T}} + (1-\alpha)\bar{\mathrm{f}}_{\mathrm{T}} \tag{20}$$

Finally, the predicted intensity function in the region of interest is calculated from (18) as follows,

$$\widetilde{\boldsymbol{\lambda}}_{\mathrm{T}+1} = \frac{\exp\left(\mathrm{E}\left(\widetilde{\boldsymbol{Y}}_{\mathrm{T}+1}\middle|\widetilde{\boldsymbol{Z}}_{\mathrm{T}-\mathrm{L}},\ldots,\widetilde{\boldsymbol{Z}}_{\mathrm{T}}\right)\right)}{\bar{\mathrm{f}}'_{\mathrm{T}+1}} \tag{21}$$

The predicted intensity function indicates the potential for pores to occur within the region of interest based on the information from previous layers. High intensity at certain locations suggests high probability of the occurrence of pores at those locations. It is utilized to characterize the spatial distribution of pores on the next layer and predict the high-risk areas prone to the occurrence of pores. By comparing the predicted porosity with the actual porosity on the next layer, the effectiveness of ALS-LGCP in characterizing the spatial correlation among pores on sequential layers and modeling the layer-wise spatial evolution of porosity is validated.

4. Application of ALS-LGCP for Layer-wise Porosity Modeling

In this section, the proposed ALS-LGCP is first illustrated with numerically generated sequences of pores, and subsequently, applied to a metal part fabricated using binder jetting AM process. The aim is to model the layer-wise spatial evolution of porosity and identify the high-risk areas in an AM part based on the estimated porosity distribution. In comparison, the spatiotemporal log Gaussian Cox process (ST-LGCP) [36] is also applied for this new application of layer-wise porosity modeling in AM part.

The validation results are compared with another benchmark method in terms of the statistical fidelity (F-score). The benchmark method employed is an empirical approach, applied by Tammas-Williams *et al*. [12], which directly uses all the pores on previous layer images for prediction and defines

the areas with pores on existing layers as the high-risk areas on the next layer.

4.1 Layer-wise spatial analysis for numerically simulated porosity data

Five sets of data with layer-wise spatially correlated pores are numerically generated from the model using Eqs. (7) - (8), where the spatial scale parameter (ϕ) and layer-wise directional scale parameter (θ) determine the correlations among the simulated pores, and the variance (σ^2) regulates the dispersion of the pores within the region of interest and across different layers. These data are simulated with the approximated parameters obtained from XCT scans of the binder jetted copper part as shown in Figure 1. Specifically, method of minimum contrast [30] is used to estimate variance and spatial scale parameters for all the layers, the means of which are then chosen as the variance $(\sigma^2 = 4)$ and the spatial scale parameter $(\phi = 10)$ for the simulated data. In addition, the layer-wise directional scale parameter (θ) is estimated by method of minimum contrast [30] too with value $(\theta = 10)$. One such set of the sequential images generated numerically is shown in Figure 6.

In the simulation, the ALS-LGCP model is trained with four layers to learn the layer-wise spatial evolution of porosity, and is validated by predicting the high-risk areas with occurrence of pores on the fifth layer based on the previous four layers. The reason for choosing the previous four layers is due to the gradual decrease in the layer-wise directional correlation between layers. The layer-wise directional correlation between layer 1 and the fifth layer in this study is decreased to ~ 0.6.

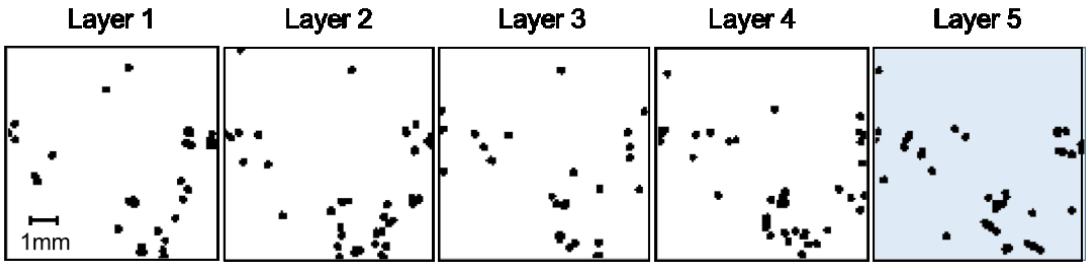

Figure 6: Representative simulation data as sequential images. The aim is to predict the high-risk areas with occurrence of pores on the fifth layer based on the previous four layers.

ALS-LGCP is used to model the obtained augmented point patterns from the simulated data in

Figure 6. Using Metropolis-adjusted Langevin algorithm (MALA), 5000 iterations of sampling are implemented for ALS-LGCP with the first 1000 iterations as burn-in period. The model converges swiftly after the burn-in period. The parameter estimates (variance σ^2, spatial scale parameter ϕ, layer-wise directional scale parameter θ) by using ALS-LGCP are summarized in

Table **2**, from which the parameters estimated by ALS-LGCP are within 8% of their true values.

Table 2: Parameter estimates (variance σ^2, spatial scale parameter ϕ, layer-wise directional scale parameter θ in Eq. (11)) using the proposed ALS-LGCP. The numbers in parenthesis are the standard deviation of the estimates (4000 iterations in MALA).

Parameter notations in the layer-wise spatial model	σ^2	ϕ	θ
True values of parameters for simulated data (Figure 6)	4	10	10
Parameter estimates using LS- LGCP	3.750 (0.730)	9.246 (0.669)	10.781 (2.897)
Relative error between the estimates and the true values	6.25%	7.54%	7.81%

With a separable covariance structure in ALS-LGCP, the spatial covariance among the pores within a layer are shown in Figure 7(a), whereas the layer-wise directional correlation among the pores across layers are shown in Figure 7(b). It is noted that both spatial correlation and layer-wise directional correlation decreases with the increasing distance within a layer and with progressive layers. Moreover, the predicted intensity function in the region of interest for the fifth layer using ALS-LGCP is shown in Figure 7(c), which indicates areas prone to porosity and their corresponding severity.

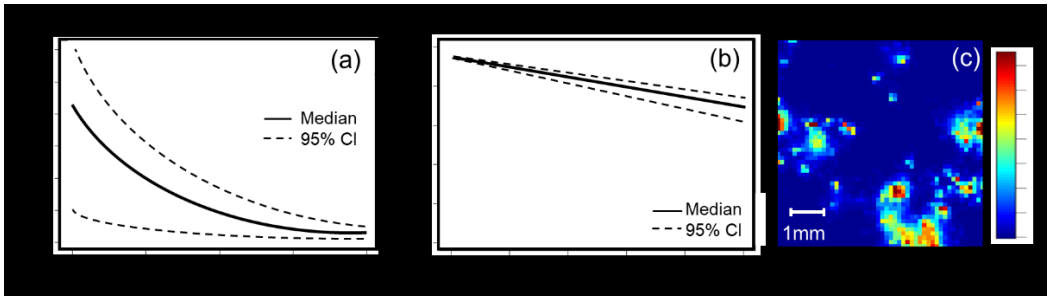

Figure 7: In the context of the simulated data in Figure 6, (a) spatial covariance of the pores along the distance,

(b) layer-wise directional correlation of the pores among sequential layers, and (c) the predicted intensity function in the region of interest for the fifth layer.

The statistical accuracy of ALS-LGCP and ST-LGCP in predicting the porosity-prone areas in the next layers is compared with the empirical approach used by Tammas-Williams *et al*. [12]. The implementation of the empirical approach for identifying high-risk areas includes three major steps: (i) Represent each layer as a binary-value matrix with value 1 at pixels of pores and value 0 otherwise; (ii) Stack the previous layers (previous four layers in this case) to from the prediction layer, a corresponding matrix of which is calculated by the total counts of the overlapped pore pixels from previous layers; (iii) Normalize this prediction matrix to 0-1 scale values, indicating the probabilities of the occurrence of pores at all the pixels. As a result, the identified high-risk areas by the three approaches are juxtaposed in Figure 8. The empirical approach overestimates the occurrence of pores by identifying overly segmented high-risk areas (Figure 8(b)); ST-LGCP underestimates the high-risk areas (Figure 8(c)); and in contrast, ALS-LGCP marks several relatively large and contiguous areas (Figure 8(d)).

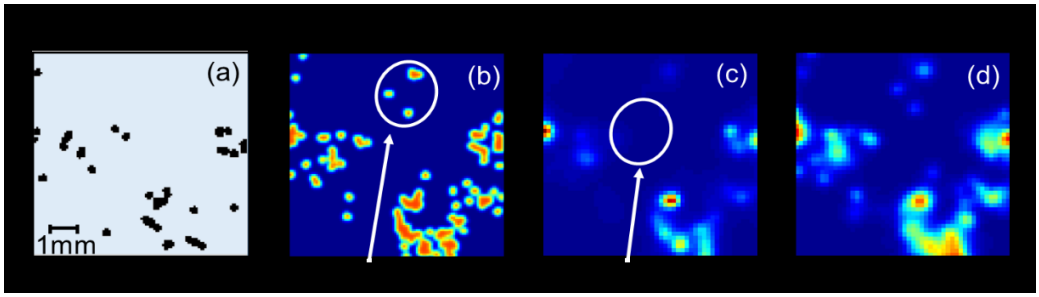

Figure 8: (a) The porosity distribution of the fifth layer; (b) overly segmented high-risk areas identified by the empirical approach (benchmark method); (c) small high-risk areas identified by ST-LGCP; and (d) relatively large and continuous high-risk areas identified by the proposed ALS-LGCP.

A statistical measure, F-score (a combination of precision and sensitivity), is used to quantify the accuracy of the three methods in predicting the porosity-prone areas on the next layer [50]. In this context, precision represents the percentage of real pores among the predicted ones, and sensitivity indicates the percentage of real pores correctly identified. Precision and sensitivity are analogous and inversely related to the Type I and Type II statistical errors, respectively. *Active cell* and *inactive cell*

are defined to calculate F-score in the discretization of ALS-LGCP.

Definition 3 (*Active cell* and *inactive cell*): An *active cell*, is a cell in the discretized region of interest that is occupied by the predicted pores with high probability; On the contrary, an *inactive cell* is deemed as the cell not occupied by the predicted pores. The following three steps are used to estimate the F-score:

1) Normalize the predicted intensity in the region of interest $\widetilde{\boldsymbol{\Lambda}}_{\mathrm{T}+1}$ in Eq. (21) into cell-wise probability of the occurrence of pores
2) Threshold the cell-wise probability by setting the probability to zero if it is smaller than the threshold for an *inactive cell* or keeping the probability value if it is larger than the threshold for an *active cell*.
3) Categorize the region within *active cells* as predicted pores, and the region within *inactive cells* as the prediction of normal condition.

With these F-score can be calculated as,

$$\begin{aligned}\text{Precision} &= \frac{\text{areas of actual } \textit{active cells} \text{ within the predicted } \textit{active cells}}{\text{total areas of predicted } \textit{active cells}}\\ \text{Sensitivity} &= \frac{\text{areas of actual } \textit{active cells} \text{ within the predicted } \textit{active cells}}{\text{total areas of actual } \textit{active cells}}\\ \text{F}-\text{score} &= 2 \times \frac{\text{Precision} \times \text{Sensitivity}}{\text{Precision} + \text{Sensitivity}}.\end{aligned} \tag{22}$$

It is noted that since the empirical approach does not generate an intensity function, probability of one is assigned to those cells with pores from previous layers, and probability of zero to the cells without pores from previous layers in the first step above. The F-score results for the total five sets of simulated sequential images are summarized in Table 3, from which it is evident that ALS-LGCP has the highest F-score in predicting high-risk areas on the next layer. The high precision and sensitivity of

ALS-LGCP substantiates the need for incorporating the pore size into modeling. In contrast, ST-LGCP, which ignores the pore size has low sensitivity, and in turn has a tendency to underestimate the porosity-prone areas. The empirical approach has very low precision, because it ignores the layer-wise spatial correlation among pores and thereby overestimates the high-risk areas. Therefore, ALS-LGCP overcomes the challenges with both existing approaches.

Table 3: F-score results for five sets of simulated data – Comparison of the empirical approach, ST-LGCP, and ALS-LGCP (The values in the parenthesis are the standard deviation for five replications).

	Empirical approach	ST-LGCP	ALS-LGCP
Precision	0.68 (0.147)	0.79 (0.085)	**0.81 (0.106)**
Sensitivity	0.96 (0.037)	0.77 (0.143)	**0.98 (0.019)**
F-score	0.79 (0.084)	0.76 (0.042)	**0.89 (0.046)**

A hypothesis test regarding whether the differences among the F-scores of the three aforementioned approaches are significant or not can be stated as:

$$H_0\text{: F-score}_{\text{(Empirical approach)}} = \text{F-score}_{\text{(ST-LGCP)}} = \text{F-score}_{\text{(ALS-LGCP)}}$$

$$H_1\text{: Not all the F-scores are the same}$$

Table 4 shows the output of the ANOVA analysis that there is a statistically significant difference in the F-scores of the three approaches for predicting the high-risk areas of pores on a layer with the significance value is 0.0058 (i.e., $p = 0.0058$), which is below the predetermined significance level of the test (i.e., $\alpha = 0.05$).

Table 4: ANOVA for comparing the empirical approach, ST-LGCP, and ALS-LGCP in terms of F-scores on five sets of simulated data. The significance level of the test is preset as $\alpha = 0.05$.

	Degree of freedom	Sum of squares	Mean Square	F	p-value
Approaches	2	0.0554	0.0277	8.177	**0.0058**
Errors	12	0.0407	0.0034		
Total	14				

In order to explore the difference among the specific approaches, multiple comparison with Tukey's pairwise comparison test is implemented here, and the outcomes from Table 5 show that ALS-LGCP significantly outperforms both the empirical approach (with $p = 0.0097$) and ST-LGCP (with $p = 0.0132$) in terms of F-scores.

Table 5: Multiple comparison with Tukey post hoc test for the empirical approach, ST-LGCP, and ALS-LGCP in terms of F-scores. The significance level of the test is preset as $\alpha = 0.05$.

(I) Approach	(J) Approach	Mean Difference (I) - (J)	95% confidence level		p-value
			Lower bound	Upper bound	
ST-LGCP	Empirical approach	0.0063	-0.0912	0.1045	0.9842
ALS-LGCP	Empirical approach	0.1320	0.0337	0.2302	**0.0097**
ALS-LGCP	ST-LGCP	0.1257	0.0275	0.2240	**0.0132**

4.2 Application of ALS-LGCP for prediction of porosity in binder jetted parts

In this case study, the effectiveness of ALS-LGCP in modeling layer-wise spatial evolution of porosity is verified with a copper part (Figure 1) made on the authors' binder jetting machine (ExOne R2). Binder jetting is an additive manufacturing process in which a liquid bonding agent is selectively deposited to join powder materials [51]. As shown in Figure 9, the jetted binder droplets interact with the powder particles to form primitives that stitch together to form a cross-sectional layer. Once a layer is deposited, a new layer of powder (~100μm thick) is recoated on top of the previous layer, which is then printed and stitched to the previous layer by the liquid binder. The layer-by-layer process is repeated to create the complete green part, which will be placed in a sintering furnace to vaporize the binder and bind the powder particles together to obtain the final product. The part may also be subjected to a secondary infiltration process with a lower melting alloy to minimize porosity. For example, copper parts are infiltrated with brass after sintering. In this work, the secondary infiltration process is not conducted.

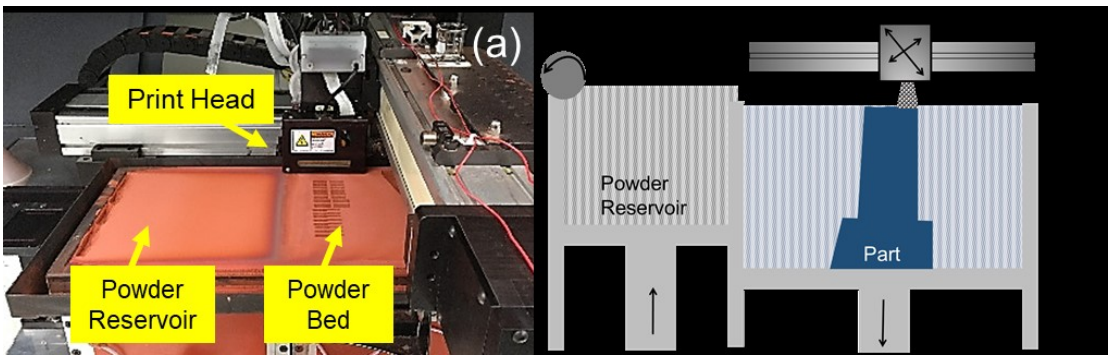

Figure 9: (a) The print head of the ExOne R2 printer; (b) the sketch of binder jetting.

The copper part with intricate features made using binder jetting was shown in Figure 1(b). XCT scanning, with resolution ~50μm, is used to visualize the internal morphology on the stem region of the part as in Figure 1(d). By aligning the scanning direction to the printing direction, the XCT scans can be related to the actual layer. XCT scans from layers 16 through 21 are shown in Figure 10. The denser material is rendered with brighter color, while hollow features and pores are darker. The layer-wise directional correlation is estimated to be at least six layers. Hence, ignoring the correlation by assuming that the pores between layers are independent is not physically tenable.

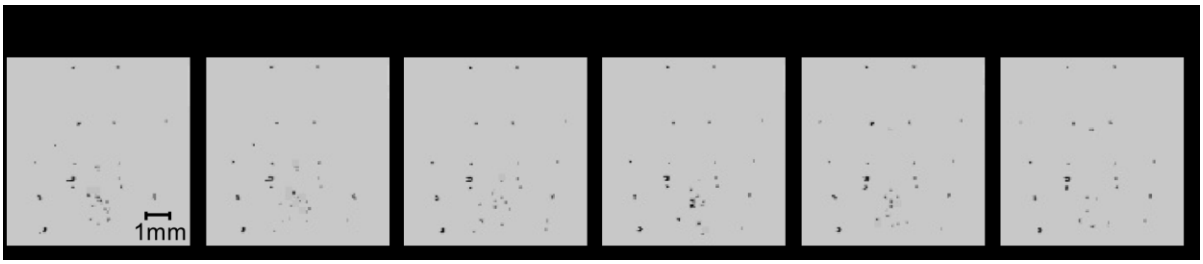

Figure 10: Sequential XCT scan images on the stem region of the copper part made in binder jetting are selected for layer-wise porosity modeling and prediction. The size of the images is about 7mm×7mm, with ~ 150×150 pixels.

In this case study, ALS-LGCP is used to model the layer-wise spatial evolution of porosity and identify the pore-prone areas in the binder jetted part. The ALS-LGCP model is validated by predicting the porosity-prone areas on the thirty images (layer 11 - layer 40) based on information from the previous six layers. This choice of the optimal number of six previous layers could be attributed to the fact that: while using less than six previous layers could cause underfitting of the model, more than six

previous layers could cause overfitting of the model, consequently, compromise the model's generalization ability in predicting the next layer. The effect of using different number of previous layers for predicting the porosity on the next layer by ALS-LGCP is shown in Figure 11, which indicates that the prediction accuracy reaches the peak average F-score value ~ 85% with six previous layers and steadily decreases thereafter. In ALS-LGCP, the images of stem region on the copper part is 150×150 pixels, and they are discretized into cells with 3×3 pixels. The parameter estimates (variance σ^2, spatial scale parameter ϕ, layer-wise directional scale parameter θ) by using ALS-LGCP are summarized in Table 6. The large value of directional scale parameter θ implies strong correlation among pores on consecutive layers.

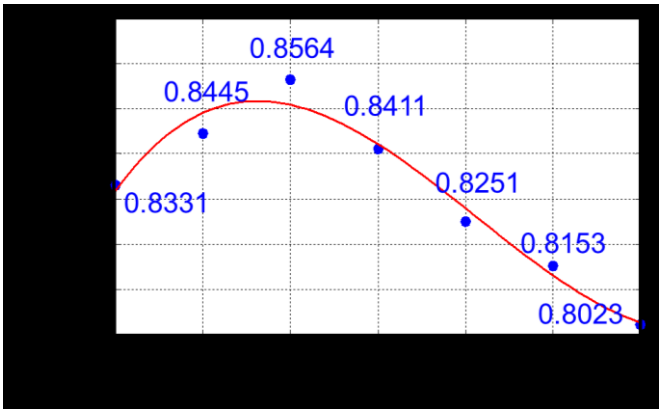

Figure 11: The average F-score results for predicting total thirty layers (layer 11 - layer 40) while using different numbers of previous layers by ALS-LGCP.

Table 6: Parameter estimates (variance σ^2, spatial scale parameter ϕ, layer-wise directional scale parameter θ in Eq. (11)) using the proposed ALS-LGCP. The numbers in parenthesis are the standard deviation of the estimates (4000 iterations in MALA).

Parameter notations	σ^2	ϕ	θ
Parameter estimates using ALS-LGCP	3.127 (0.346)	14.210 (1.286)	20.466 (3.747)

As a demonstration, ALS-LGCP is applied on the obtained augmented point patterns from the images (layer 16 - layer 21) in Figure 10 for layer-wise spatial analysis of porosity evolution. The predicted high-risk areas on layer 22 by ALS-LGCP, ST-LGCP and the empirical approach are shown

in Figure 12 for comparison. The empirical approach identifies the segmented porosity-prone areas (Figure 12(b)) by directly using all the pores from previous layers for prediction. ST-LGCP finds relatively large areas with low local intensity (Figure 12(c)) in that it reduces pores into dimensionless points; hence it tends to underestimate the severity of the pores. In contrast, ALS-LGCP marks relatively large and continuous areas with high local intensity (Figure 12(d)) by accounting for the size of the pores and also the decrease in layer-wise directional correlation among previous images (layers).

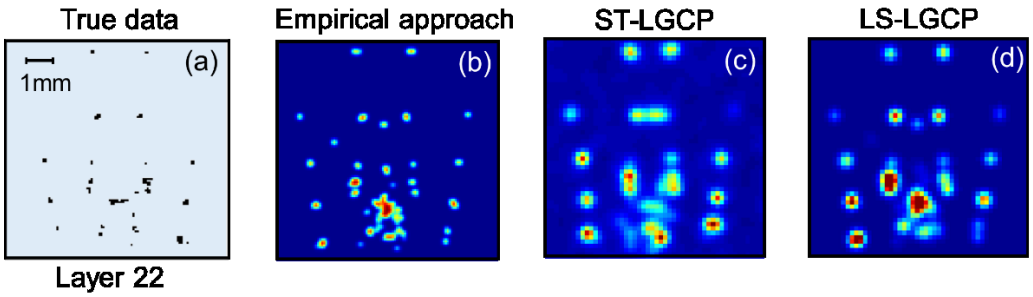

Figure 12: (a) The pores on the layer 22; (b) overly segmented high-risk areas identified by the empirical approach (benchmark method); (c) high-risk areas with low local intensity identified by ST-LGCP; and (d) high-risk areas with high local intensity identified by the proposed ALS-LGCP.

The F-score results for predicting the porosity for total thirty layers (layer 11 - layer 40) are summarized in Table 7. ALS-LGCP has ~ 5% higher F-score in predicting high-risk areas on the next layer than the two methods. It is also noted that the performance of ST-LGCP improves in this practical case study since small pores could cater for its assumption of dimensionless points.

Table 7: F-score results for predicting total thirty layers (layer 11 - layer 40) – Comparison of the empirical approach, ST-LGCP, and ALS-LGCP (The values in the parenthesis are the standard deviation).

	Empirical approach	ST-LGCP	ALS-LGCP
Precision	0.77 (0.144)	0.72 (0.123)	**0.79 (0.105)**
Sensitivity	0.85 (0.119)	0.94 (0.058)	**0.95 (0.056)**
F-score	0.80 (0.109)	0.81 (0.090)	**0.86 (0.064)**

The outputs of the ANOVA analysis in Table 8 indicate that there is a statistically significant difference in the F-scores of the three approaches for predicting the high-risk areas of pores on a layer with the significance value is 0.0292 (i.e., $p = 0.0058$), which is below the predetermined significance

level of the test (i.e., α = 0.05). Furthermore, the results of the multiple comparison with Tukey post hoc test in Table 9 show that ALS-LGCP significantly surpasses the empirical approach in identifying the pore-prone areas in terms of F-score (with $p = 0.0442$), and it also outperforms ST-LGCP but not to a statistical significant extent (with $p = 0.0579$).

Table 8: ANOVA for comparing the empirical approach, ST-LGCP, and ALS-LGCP in terms of F-scores on predicting total thirty layers (layer 11 - layer 40). The significance level of the test is preset as α = 0.05.

	Degree of freedom	Sum of squares	Mean Square	F	p-value
Approaches	2	0.0616	0.0308	3.682	**0.0292**
Errors	87	0.7282	0.0084		
Total	89				

Table 9: Multiple comparison with Tukey post hoc test for the empirical approach, ST-LGCP, and ALS-LGCP in terms of F-scores on predicting total thirty layers (layer 11 - layer 40). The significance level of the test is preset as $\alpha = 0.05$.

(I) Approach	(J) Approach	Mean Difference (I) - (J)	95% confidence level		p-value
			Lower bound	Upper bound	
ST-LGCP	Empirical approach	-0.0043	-0.0606	0.0520	0.9820
ALS-LGCP	Empirical approach	0.0575	0.0012	0.1138	**0.0442**
ALS-LGCP	ST-LGCP	0.0532	-0.0011	0.1096	0.0579

From these results, it is evident the proposed ALS-LGCP achieves superior predictions about the location and severity of porosity in AM parts. These results are important from a practical perspective, since accurate prediction of where and which layer pores are liable to occur is the first-step towards a prescription for improving the part design and optimizing the building conditions [52, 53].

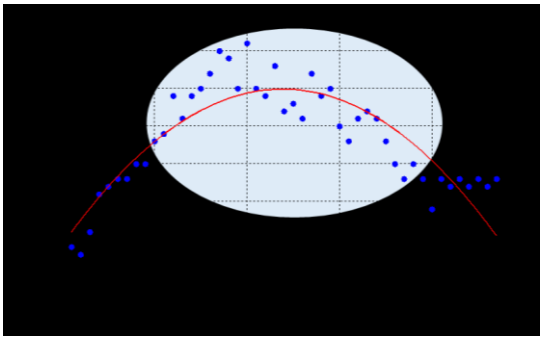

Figure 13: The number of pores within the selected region on each layer is the range of layers (layer 10 - layer 40) are used for layer-wise porosity prediction.

Continuing with the analysis by applying ALS-LGCP on layers (layer 1 – layer 50) of the binder jetted part, the expected number of pores on each layer is estimated through Eq. (9) and illustrated in Figure 13, together with a fitted trend. It is noticeable that porosity in the middle layers (shaded in Figure 13) tends to be worse. The proposed ALS-LGCP approach thus leads to an understanding of porosity within a layer, as well as across layers in AM. In other words, it provides accurate quantification for pore distribution in 3D space and leads to the insights of the layer's effect on material properties. Consequently, the results from ALS-LGCP will be instrumental for porosity reduction in future printed parts by further process or design optimization. To extend this further,

1) ALS-LGCP can distinguish common-cause porosity from those caused by unexpected process defects (special cause), such as nozzle clogs. By systematically quantifying the spatial and layer-wise distribution of porosity from XCT data, compared to other porosity measurement techniques such as density measurement, it is possible to isolate the material and process phenomena that are at the root of porosity. The proposed ALS-LGCP model in this work indeed reveals the underlying trend in porosity occurrence due to faults in the manufacturing process as shown in Figure 13.
2) ALS-LGCP can be used to study the porosity distribution of large artifacts made in AM. The attenuation of X-ray in high element number materials (e.g. copper) typically leads to a dimensional limitation of the sample when subjected to XCT scanning. As a result, the scanning of a large artifact can lead to a requirement of higher power, longer scanning time, and compromised resolution. When the overall porosity of a large artifact needs to be understood but is difficult to obtain, a small section or specific features of the part can be studied by XCT scanning. The obtained porosity data (e.g., the pore numbers and distributions in Figure 12 and Figure 13) can subsequently be used to estimate the porosity in the un-scanned sections of this large artifact

using the proposed ALS-LGCP model through extrapolation.

5. Conclusions and Future Work

This research advances an augmented layer-wise spatial log Gaussian Cox process (ALS-LGCP) to understand and model the layer-wise spatial behavior of pore formation in additive manufacturing. Specifically, the ALS-LGCP model first represents the pores observed from XCT scan images of an AM product with augmented point patterns, including the information about the number, location, and size of the pores. It further utilizes the spatial correlations among the pores for identifying areas susceptible to pores on different layers. In this work, the ALS-LGCP approach is applied to parts made using binder jetting where it locates the areas vulnerable to porosity with statistical fidelity approaching ~ 85% (F-score).

Accordingly, this work presents a consequential analytical direction to understand and quantify porosity in AM parts. From the methodological vista, the proposed augmented point pattern approach incorporates not only the locations, but also the morphological features of pores, such as their size and form, into the analysis. Therefore, ALS-LGCP is capable of accurately estimating the intensity function to describe the pore distribution. From the practical application point of view, to the best of our knowledge, the ALS-LGCP is perhaps the first work using layer-wise 3D spatial model to quantify the porosity of AM parts. It is therefore a significant improvement over the current scalar metric (percentage porosity by volume) used to quantify porosity, namely, the percentage porosity relative to the bulk part volume.

By evaluating the quality of AM parts in a layer-wise manner, it has a promising potential for quality improvement and process optimization by adjusting process parameters and part design contingent on the porosity on different layers. The practical outcome is that porosity-prone areas of a part can be

ascertained based on a few test parts, and the appropriate design or process parameters can be modified for scale production or larger artifacts. Given its data-driven nature, it is posited that the proposed approach can be readily generalized to different powder-based AM processes.

The authors' forthcoming research will focus on addressing the following three unresolved aspects of this work:

- Verifying the repeatability of ALS-LGCP for porosity modeling from different AM processes.
- Diagnosing the physical reason for the distribution of porosity with particular forms in AM parts, and testing remedies to eliminate porosity either by optimizing the part design or process parameters.
- Incorporating online quality assurance in AM with *in-situ* XCT scanner or high-resolution cameras.

Acknowledgement:

This project was funded by the following grants from the National Science Foundation (NSF): CMMI No. 1254287, CMMI No. 1436592, and CMMI No. 1752069.

References

[1] N. Guo and M. C. Leu, "Additive manufacturing: technology, applications and research needs," *Frontiers of Mechanical Engineering,* vol. 8, pp. 215-243, 2013.

[2] W. E. Frazier, "Metal additive manufacturing: A review," *Journal of Materials Engineering and Performance,* vol. 23, pp. 1917-1928, 2014.

[3] M. Grasso and B. M. Colosimo, "Process defects and in situ monitoring methods in metal powder bed fusion: a review," *Measurement Science and Technology,* vol. 28, p. 044005, 2017.

[4] W. J. Sames, F. List, S. Pannala, R. R. Dehoff, and S. S. Babu, "The metallurgy and processing science of metal additive manufacturing," *International Materials Reviews,* vol. 61, pp. 315-360, 2016.

[5] I. Gibson, D. Rosen, and B. Stucker, *Additive manufacturing technologies* vol. 238. New York: Springer, 2010.

[6] D. Bourell, J. P. Kruth, M. Leu, G. Levy, D. Rosen, A. M. Beese*, et al.*, "Materials for additive manufacturing," *CIRP Annals-Manufacturing Technology,* 2017.

[7] A. Spierings and G. Levy, "Comparison of density of stainless steel 316L parts produced with selective laser melting using different powder grades," in *Proceedings of the Annual International Solid Freeform Fabrication Symposium*, 2009, pp. 342-353.

[8] I. Yadroitsev and I. Smurov, "Selective laser melting technology: from the single laser melted track stability to 3D parts of complex shape," *Physics Procedia,* vol. 5, pp. 551-560, 2010.

[9] C. Zhao, K. Fezzaa, R. W. Cunningham, H. Wen, F. Carlo, L. Chen*, et al.*, "Real-time monitoring of laser powder bed fusion process using high-speed X-ray imaging and diffraction," *Scientific reports,* vol. 7, p. 3602, 2017.

[10] C. Kenel, D. Grolimund, X. Li, E. Panepucci, V. Samson, D. F. Sanchez*, et al.*, "In situ investigation of phase transformations in Ti-6Al-4V under additive manufacturing conditions combining laser melting and high-speed micro-X-ray diffraction," *Scientific reports,* vol. 7, p. 16358, 2017.

[11] S. Siddique, M. Imran, M. Rauer, M. Kaloudis, E. Wycisk, C. Emmelmann*, et al.*, "Computed tomography for characterization of fatigue performance of selective laser melted parts," *Materials & Design,* vol. 83, pp. 661-669, 2015.

[12] S. Tammas-Williams, H. Zhao, F. Léonard, F. Derguti, I. Todd, and P. Prangnell, "XCT analysis of the influence of melt strategies on defect population in Ti–6Al–4V components manufactured by Selective Electron Beam Melting," *Materials Characterization,* vol. 102, pp. 47-61, 2015.

[13] J. A. Slotwinski, E. J. Garboczi, and K. M. Hebenstreit, "Porosity Measurements and Analysis for Metal Additive Manufacturing Process Control," *JOURNAL OF RESEARCH OF THE NATIONAL INSTITUTE OF STANDARDS AND TECHNOLOGY,* vol. 119, pp. 494-528, 2014.

[14] S. Leuders, M. Thöne, A. Riemer, T. Niendorf, T. Tröster, H. Richard*, et al.*, "On the mechanical behaviour of titanium alloy TiAl6V4 manufactured by selective laser melting: Fatigue resistance and crack growth performance," *International Journal of Fatigue,* vol. 48, pp. 300-307, 2013.

[15] H. Gong, K. Rafi, T. Starr, and B. Stucker, "The Effects of Processing Parameters on Defect Regularity in Ti-6Al-4V Parts Fabricated By Selective Laser Melting and Electron Beam Melting," presented at the 24th Annual International Solid Freeform Fabrication Symposium—An Additive Manufacturing Conference, Austin, TX, 2013.

[16] C. B. Williams, J. K. Cochran, and D. W. Rosen, "Additive manufacturing of metallic cellular materials via three-dimensional printing," *The International Journal of Advanced Manufacturing Technology,* vol. 53, pp. 231-239, 2011.

[17] Y. Bai and C. B. Williams, "An exploration of binder jetting of copper," *Rapid Prototyping Journal,* vol. 21, pp. 177-185, 2015.

[18] S. Gaytan, M. Cadena, H. Karim, D. Delfin, Y. Lin, D. Espalin*, et al.*, "Fabrication of barium titanate by binder jetting additive manufacturing technology," *Ceramics International,* vol. 41, pp. 6610-6619, 2015.

[19] A. Spierings, M. Schneider, and R. Eggenberger, "Comparison of density measurement techniques for additive manufactured metallic parts," *Rapid Prototyping Journal,* vol. 17, pp. 380-386, 2011.

[20] D. Bourell, B. Stucker, A. Spierings, N. Herres, and G. Levy, "Influence of the particle size distribution on surface quality and mechanical properties in AM steel parts," *Rapid Prototyping Journal,* vol. 17, pp. 195-202, 2011.

[21] N. Karthik, H. Gu, D. Pal, T. Starr, and B. Stucker, "High Frequency Ultrasonic Non Destructive Evaluation of Additively Manufactured Components," in *Proceeding of the Twenty Forth Annual International Solid Freeform Fabrication Symposium*, 2013, pp. 311-325.

[22] K. Monroy, J. Delgado, and J. Ciurana, "Study of the pore formation on CoCrMo alloys by selective laser melting manufacturing process," *Procedia Engineering,* vol. 63, pp. 361-369, 2013.

[23] H. Gu, H. Gong, D. Pal, K. Rafi, T. Starr, and B. Stucker, "Influences of energy density on porosity and microstructure of selective laser melted 17-4PH stainless steel," in *2013 Solid Freeform Fabrication Symposium*, 2013, p. 474.

[24] F. Léonard, S. Tammas-Wiliams, P. B. Prangnell, I. Todd, and P. J. Withers, "Assessment by X-ray CT of the effects of geometry and build direction on defects in titanium ALM parts," in *Conference on Industrial Computed Tomography (ICT)*, 2012, pp. 85-93.

[25] E. Girardin, C. Renghini, J. Dyson, V. Calbucci, F. Moroncini, and G. Albertini, "Characterization of porosity in a laser sintered MMCp using X-ray synchrotron phase contrast microtomography," *Materials Sciences and Applications,* vol. 2, p. 1322, 2011.

[26] B. Sharrat, "Non-Destructive Techniques and Technologies for Qualification of Additive Manufactured Parts and Processes: A Literature Review," Defence Research and Development Canada,2015.

[27] A. Thompson, I. Maskery, and R. K. Leach, "X-ray computed tomography for additive manufacturing: a review," *Measurement Science and Technology,* vol. 27, p. 072001, 2016.

[28] H. Taud, R. Martinez-Angeles, J. Parrot, and L. Hernandez-Escobedo, "Porosity estimation method by X-ray computed tomography," *Journal of Petroleum Science and Engineering,* vol. 47, pp. 209-217, 2005.

[29] F. Kim, S. Moylan, E. Garboczi, and J. Slotwinski, "Investigation of pore structure in cobalt chrome additively manufactured parts using X-ray computed tomography and three-dimensional image analysis," *Additive Manufacturing,* vol. 17, pp. 23-38, 2017.

[30] N. Cressie and C. K. Wikle, *Statistics for spatio-temporal data*: John Wiley & Sons, 2011.

[31] S. Banerjee, B. P. Carlin, and A. E. Gelfand, *Hierarchical modeling and analysis for spatial data*: Crc Press, 2014.

[32] D. Stoyan and A. Penttinen, "Recent applications of point process methods in forestry statistics," *Statistical Science,* pp. 61-78, 2000.

[33] Y. Ogata, "Space-time point-process models for earthquake occurrences," *Annals of the Institute of Statistical Mathematics,* vol. 50, pp. 379-402, 1998.

[34] Q. Zhou, J. Zhou, M. De Cicco, S. Zhou, and X. Li, "Detecting 3D spatial clustering of particles in nanocomposites based on cross-sectional images," *Technometrics,* vol. 56, pp. 212-224, 2014.

[35] L. Dong, X. Li, Y. Qian, D. Yu, H. Zhang, Z. Zhang*, et al.*, "Quantifying Nanoparticle Mixing State to Account for Both Location and Size Effects," *Technometrics,* vol. 0, pp. 1-13, 2017.

[36] A. Brix and P. J. Diggle, "Spatiotemporal prediction for log-Gaussian Cox processes," *Journal of the Royal Statistical Society: Series B (Statistical Methodology),* vol. 63, pp. 823-841, 2001.

[37] J. Møller, A. R. Syversveen, and R. P. Waagepetersen, "Log gaussian cox processes," *Scandinavian journal of statistics,* vol. 25, pp. 451-482, 1998.

[38] Y. Li and Y. Guan, "Functional principal component analysis of spatiotemporal point processes with applications in disease surveillance," *Journal of the American Statistical Association,* vol. 109, pp. 1205-1215, 2014.

[39] Y. Li, P. Brown, D. C. Gesink, and H. Rue, "Log Gaussian Cox processes and spatially aggregated disease incidence data," *Statistical methods in medical research,* vol. 21, pp. 479-507, 2012.

[40] J. Ahn, T. D. Johnson, D. Bhavnani, J. N. Eisenberg, and B. Mukherjee, "A space-time point process model for analyzing and predicting case patterns of diarrheal disease in northwestern Ecuador," *Spatial and spatio-temporal epidemiology,* vol. 9, pp. 23-35, 2014.

[41] G. Mohler, "Modeling and estimation of multi-source clustering in crime and security data," *The Annals of Applied Statistics,* vol. 7, pp. 1525-1539, 2013.

[42] L. Serra, M. Saez, J. Mateu, D. Varga, P. Juan, C. Díaz-Ávalos*, et al.*, "Spatio-temporal log-Gaussian Cox processes for modelling wildfire occurrence: the case of Catalonia, 1994–2008," *Environmental and ecological statistics,* vol. 21, pp. 531-563, 2014.

[43] A. Iftimi, O. Cronie, and F. Montes, "The second-order analysis of marked spatio-temporal point processes, with an application to earthquake data," *arXiv preprint arXiv:1611.04808,* 2016.

[44] N. T. Aboulkhair, N. M. Everitt, I. Ashcroft, and C. Tuck, "Reducing porosity in AlSi10Mg parts processed by selective laser melting," *Additive Manufacturing,* vol. 1, pp. 77-86, 2014.

[45] B. M. Taylor, T. M. Davies, B. S. Rowlingson, and P. J. Diggle, "lgcp: An R Package for Inference with Spatio-Temporal Log-Gaussian Cox Processes," *arXiv preprint arXiv:1110.6054,* 2011.

[46] B. Taylor, T. Davies, B. Rowlingson, and P. Diggle, "Bayesian inference and data augmentation schemes for spatial, spatiotemporal and multivariate Log-Gaussian Cox processes in R," *Journal of Statistical Software,* vol. 63, pp. 1-48, 2015.

[47] N. Metropolis, A. W. Rosenbluth, M. N. Rosenbluth, A. H. Teller, and E. Teller, "Equation of state calculations by fast computing machines," *Journal of Chemical Physics,* vol. 21, pp. 1087-1092, 1953.

[48] W. K. Hastings, "Monte Carlo sampling methods using Markov chains and their applications," *Biometrika,* vol. 57, pp. 97-109, 1970.

[49] G. O. Roberts and R. L. Tweedie, "Exponential convergence of Langevin distributions and their discrete approximations," *Bernoulli,* pp. 341-363, 1996.

[50] D. M. Powers, "Evaluation: from precision, recall and F-measure to ROC, informedness, markedness and correlation," *Journal of Machine Learning Technologies,* vol. 2, pp. 37-63, 2011.

[51] ISO/ASTM, "ISO/ASTM 52900: Additive manufacturing-General principles-Terminology," ed, 2015, pp. 1-19.

[52] M. P. Meeder, "Modeling the Thermal and Electrical Properties of Different Density Sintered Binder Jetted Copper for Verification and Revision of The Wiedemann-Franz Law," Master's thesis, Mechanical Engineering, Virginia Tech, 2016.
[53] J. Koh and A. Fortini, "Prediction of thermal conductivity and electrical resistivity of porous metallic materials," *International Journal of Heat and Mass Transfer,* vol. 16, pp. 2013-2022, 1973.

Bio Sketches:

Jia (Peter) Liu

Chenang Liu received his double B.S. degrees in environmental & resource sciences and mathematics from Zhejiang University, China, in 2014, and his M.S. degree in statistics from Virginia Tech in 2017, respectively. He is currently a Ph.D. candidate in the Grado department of industrial and systems engineering at Virginia Tech. His current research focuses on advanced data analytics for online quality assurance of advanced manufacturing.

Yun Bai received his B.S. degree from Missouri University of Science and Technology in 2013, and Ph.D. degree from Virginia Tech in 2018, both in mechanical engineering. He is currently a process engineer with Desktop Metal, Burlington, MA. His research interests include material and process development for Additive Manufacturing.

Prahalad Rao earned his B.Tech degree in 2003 specializing in Production Engineering (First Class) from Victoria Jubilee Technical Institute (VJTI), Bombay University, India. He received his M.S. and Ph.D. degrees in Industrial Engineering from Oklahoma State University in 2006 and 2013, respectively. He is currently an Assistant Professor in the Mechanical and Materials Engineering Department at University of Nebraska-Lincoln. His research focuses on sensor-based monitoring of complex systems , e.g., additive manufacturing, ultraprecision manufacturing, and neurophysiology. He earned the 2017 Society of Manufacturing Engineers, Yoram Koren Outstanding Young Manufacturing Engineer Award, and the 2018 IISE Transactions Best Paper Award. He has published over 25 peer-reviewed journal articles. His research has received three grants from the National science foundation (NSF) in the last 4 years, including the NSF CAREER award in 2018.

Christopher B. Williams is an Associate Professor and Electro Mechanical Corporation Faculty Fellow in the Department of Mechanical Engineering at Virginia Tech. He is the Director of the Design, Research, and Education for Additive Manufacturing Systems (DREAMS) Laboratory and Associate Director of the Macromolecules Innovation Institute (MII). His research spans the value chain of Additive Manufacturing, from process-structure-property relationships of novel materials to process cyber-physical security. His contributions have been recognized by eight Best Paper awards at international design, manufacturing, and engineering education conferences. He is a recipient of a National Science Foundation CAREER Award in 2013 and the International Outstanding Young Researcher in Freeform and Additive Fabrication Award in 2012. He serves on the Additive Manufacturing Community Advisors for SME. Chris holds a Ph.D. and M.S. from the Georgia

Institute of Technology, and a B.S. with High Honors from the University of Florida, in Mechanical Engineering.

Zhenyu (James) Kong received the B.S. and M.S. degrees in mechanical engineering from the Harbin Institute of Technology, Harbin, China, in 1993 and 1995, respectively, and the Ph.D. degree from the Department of Industrial and System Engineering, University of Wisconsin–Madison, in 2004. He is currently an Associate Professor in the Grado Department of Industrial and Systems Engineering at Virginia Tech. He is the Director of Smart Manufacturing Analytics Research and Technology (SMART) Laboratory. His research interests include sensing and analytics for smart manufacturing, and modeling, synthesis, and diagnosis for large and complex manufacturing systems. His research contributions have been recognized by six Best Paper awards in international research conferences and IISE Transactions.